Supporting Information

Fish Gill Inspired Crossflow for Efficient and Continuous Collection of Spilled Oil

Yuhai Dou,[†] Dongliang Tian,[†,‡] Ziqi Sun,*[†,§] Qiannan Liu,[†] Na Zhang,[‡] Jung Ho Kim,[†] Lei Jiang,[‡,⊥] and Shi Xue Dou[†]*

[†]Institute for Superconducting and Electronic Materials, Australian Institute for Innovative Materials, University of Wollongong, Wollongong, New South Wales 2500, Australia

[‡]Key Laboratory of Bio-Inspired Smart Interfacial Science and Technology of the Ministry of Education, School of Chemistry and Environment, Beihang University, Beijing 100191, P. R. China

[§]School of Chemistry, Physics and Mechanical Engineering, Queensland University of Technology, Brisbane, Queensland 4001, Australia

[⊥]Technical Institute of Physics and Chemistry, Chinese Academy of Sciences, Beijing 100191, P. R. China

*Coresponding Authors. E-mail: tiandl@buaa.edu.cn; ziqi.sun@qut.edu.au

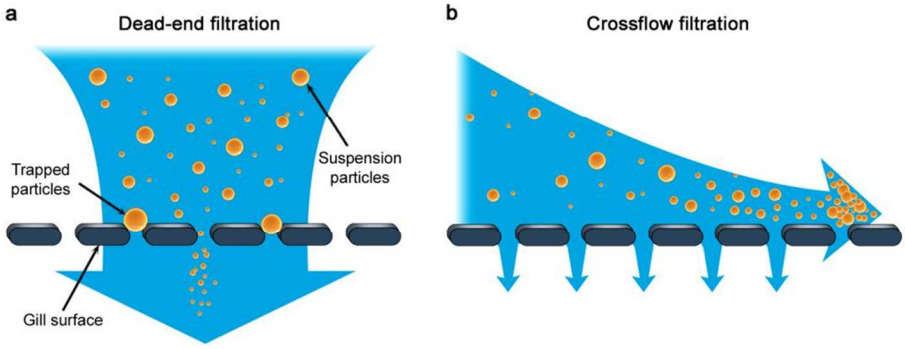

Figure S1. Schematic illustration of dead-end and crossflow filtration in fish gills. (Reproduced with permission from ref. 1. Copyright 2001 Nature Publishing Group) a) In dead-end filtration, the fluid flows perpendicularly to the gill surface. As water leaves through the spaces, the gill is easily clogged by food particles. b) In crossflow filtration, the fluid flows parallel to the gill surface. Water is strained through the spaces, while food particles are concentrated and transported to the oesophagus. Most of the particles do not come into contact with the gill surface but remain suspended, thus effectively avoiding clogging of the gill.

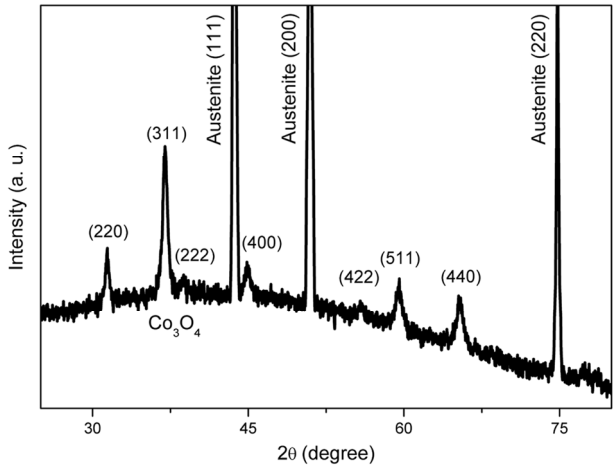

Figure S2. XRD pattern of the ultrathin Co_3O_4 nanosheets-coated membrane. The well-crystallized cubic Co_3O_4 phase of the coated nanosheets and the austenite phase of the stainless steel mesh are clearly detected.

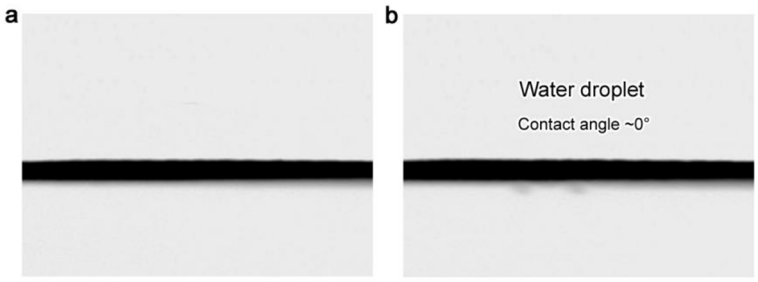

Figure S3. Superhydrophilicity of ultrathin Co_3O_4 nanosheets-coated surface. a) Ultrathin Co_3O_4 nanosheets-coated stainless steel sheet. b) A water droplet (3 μL) deposited on the sheet shows a contact angle of ~0°, indicating the superhydrophilicity of the surface.

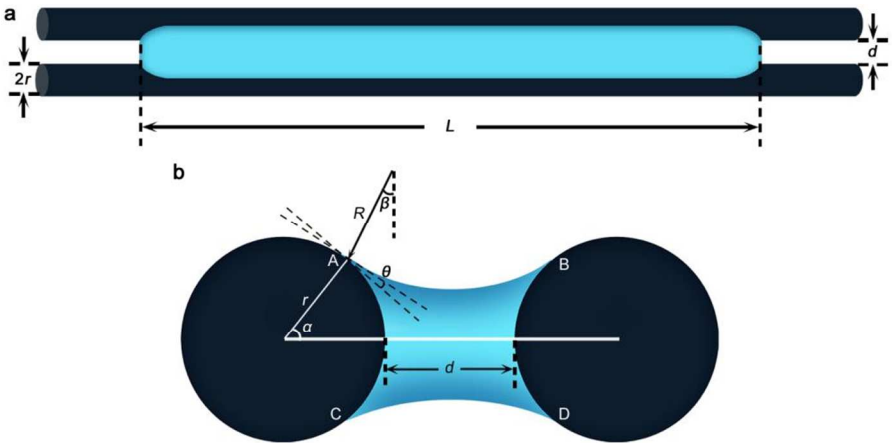

Figure S4. Water layer on two parallel horizontal wires. a) Overall view. b) Cross-sectional view.

Derivation of the equilibrium condition. To determine the final spreading state of the water layer in Figure S4, we assume that adding more water into the layer changes only L (the length of the water layer), but not α (the angle between the line connecting the wire centers and the radius to the air-water-solid boundary) or R (the curvature of the water surface). In addition, the increase in free energy (dF) associated with the increase in the length of the water layer by dL must be equal to the work (dW) done on the system. The free energy change is caused by the wetting of the originally nonwetted wires $(D_{AC} + D_{BD})$dL, and the creation of a free water surface $(D_{AB} + D_{CD})$dL:

$$dF = [(D_{AC} + D_{BD})(\gamma_{SL} - \gamma_{SV}) + (D_{AB} + D_{CD})\gamma]dL \quad (1)$$

where D is the distance between two air-water-solid boundaries, γ is the surface tension of water, γ_{SL} and γ_{SV} are the wire/water and wire/gas interfacial tensions, respectively. According to Young:[2]

$$\gamma_{SV} - \gamma_{SL} = \gamma\cos\theta$$

Meanwhile $D_{AB} = D_{CD} = 2(\pi/2 - \theta - \alpha)R$ and $D_{AC} = D_{BD} = 2\alpha r$ (where θ is the water contact angle on the wire surface, and r is the radius of the wire), so Equation (1) can be written as

$$dF = [4(\pi/2 - \theta - \alpha)R - 4\alpha r\cos\theta]\gamma dL \quad (2)$$

To obtain the work (dW) done on the system, the pressure applied on the water layer is first studied. According to the force-balance principle, we obtain that

$$(P_1 - P_2)D_{AB}L = 2\gamma\sin\beta L \quad (3)$$

where P_1 and P_2 are the pressures outside and inside the water layer, respectively, and β is the angle between the radius from the center of the meniscus to the air-water-solid boundary and the line perpendicular to the line connecting the wire centers. From simple geometry, it follows that

$$\sin\beta = D_{AB}/2R$$

so Equation (3) can be written:

$$P_1 - P_2 = \gamma/R$$

When the length of the water layer is increased by dL, the work done on the system is

$$dW = (P_2 - P_1)S_{ABCD}dL = -\gamma S_{ABCD}dL/R$$

here, S_{ABCD} is the cross-sectional area of the water layer that is given by

$$S_{ABCD} = 2r^2\{2(R/r)\sin\alpha\cos(\theta + \alpha) - \alpha + \sin\alpha\cos\alpha - (R/r)^2[(\pi/2 - \theta - \alpha) - \sin(\theta + \alpha)\cos(\theta + \alpha)]\}$$

Therefore,

$$dW = -2\gamma r^2 dL\{2(R/r)\sin\alpha\cos(\theta + \alpha) - \alpha + \sin\alpha\cos\alpha - (R/r)^2[(\pi/2 - \theta - \alpha) - \sin(\theta + \alpha)\cos(\theta + \alpha)]\}/R \quad (4)$$

By combining Equations (2) and (4), we obtain the equilibrium condition:

$$(R/r)^2[\pi/2 - \theta - \alpha + \sin(\theta + \alpha)\cos(\theta + \alpha)] + 2(R/r)[\sin\alpha\cos(\theta + \alpha) - \alpha\cos\theta] + \sin\alpha\cos\alpha - \alpha = 0.$$

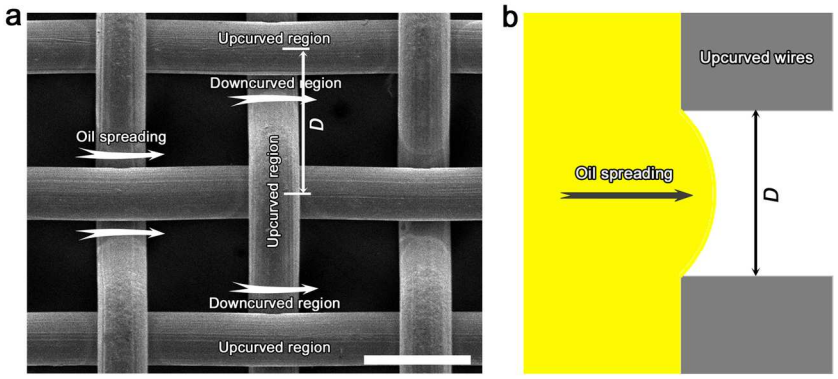

Figure S5. Lateral pinning effect of water-wetted wires. a) Stainless steel mesh woven by interlacing the warp and welf wires, forming upcurved region and downcurved region (scale bar: 100 μm). b) Illustration of pinning effect of upcurved water-wetted wires on lateral oil spreading.

Explanation of lateral pinning effect of the water-wetted wires. Oil is difficult to spread to the site on account of the maximum pressure P_{max}, which can sustain a straight stream between the curved surface of the wires and is given by the following equation:[3]

$$P_{max} = \gamma/R = \gamma[2\sin(\theta - \pi/2)]/D$$

where γ is the surface tension of the oil on water-wetted wires, D is the spacing of the upcurved surface of the wires, and θ is the advancing contact angle of oil on the surface. Therefore, a decrease in D leads to an increase in P_{max}, indicating that stronger pinning effect and less oil spreading on small-pore membranes.

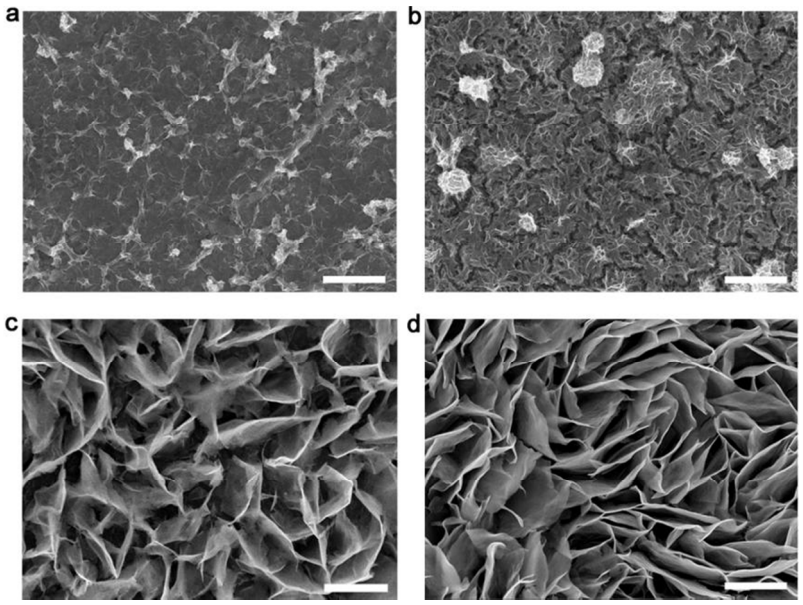

Figure S6. SEM images of the coated nanostructures with different cell sizes. These structures were prepared by varying the H_2O addition in precursor solutions. a) 0 g H_2O. b) 0.5 g. c) 2.0 g. d) 4.0 g. Scale bars: 1 μm.

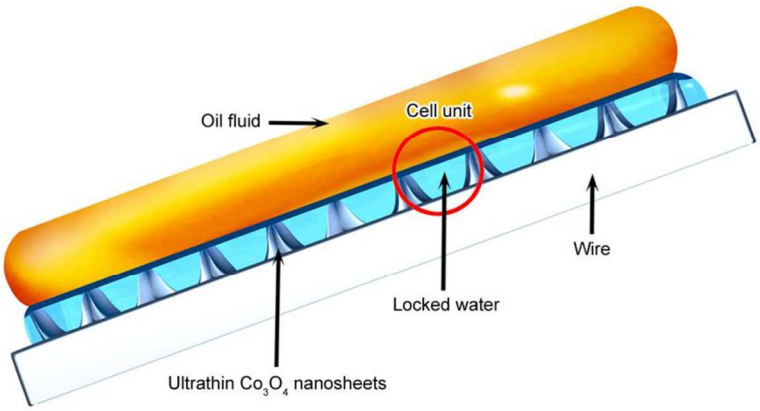

Figure S7. Oil repellency of the ultrathin Co_3O_4 nanosheets-coated wire surface. The Co_3O_4 nanosheets can firmly lock water inside the enclosed cells, forming a robust water-sequestering and oil-repelling layer for easy oil transportation and collection.

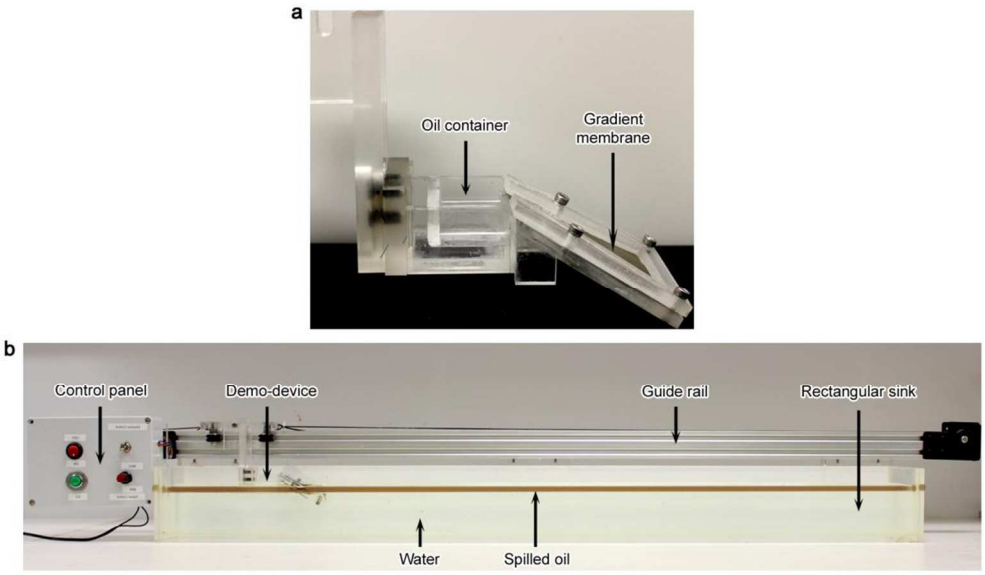

Figure S8. Demonstration device and apparatus for crossflow collection of spilled oil. a) The device consists of a gradient membrane and an oil container. b) The apparatus is made up of a rectangular sink, a guide rail, a motor and a control panel. The guide rail was installed at one side of the rectangular sink to provide the device with smooth and quiet motion. The device was driven by the motor with the panel programmed to control its movement. For the demonstration, water and oil were first poured into the sink to simulate a real oil spill in the environment, and then the device was driven to move along the oil/water interface and collect the spilled oil.

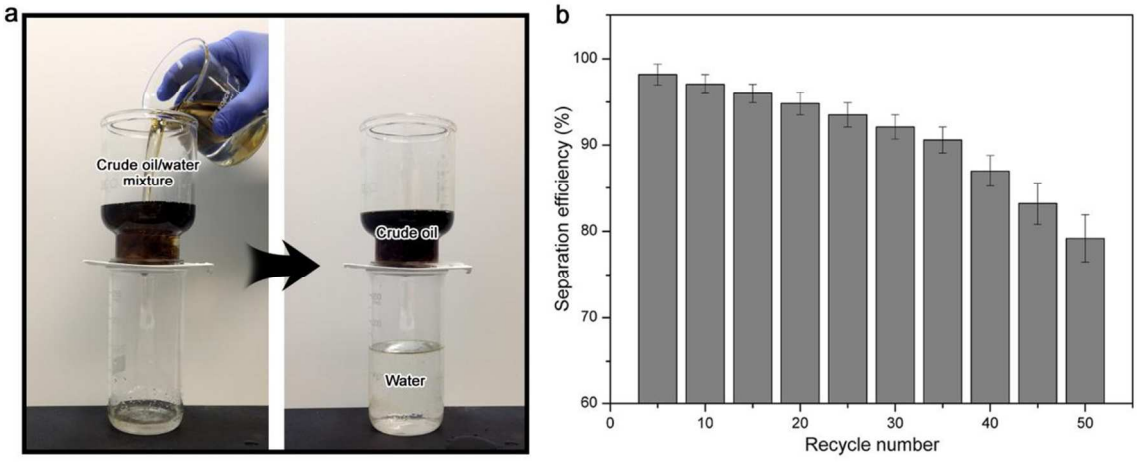

Figure S9. Gravity-driven crude oil/water separation (90 μm membrane). a) Dynamic separation process. b) Separation efficiency as a function of recycle number. The separation efficiencies were calculated using the equation: $Q_G(\%) = (1 - C_p/C_o) \times 100$ (C_o and C_p are the oil concentration in original oil/water mixture and separated water, respectively).

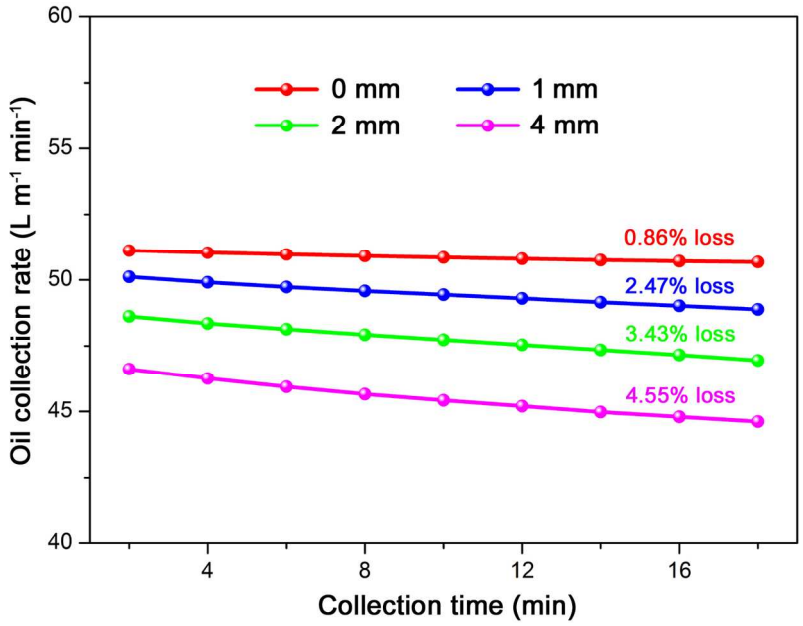

Figure S10. Effect of wave height on the collection of spill oil collection (device speed, 0.4 m s^{-1}). The oil collection rate declines much more quickly with increasing wave height, indicating the adverse effect of surface waves.

Table S1. *d*/2*r* values of the five component parts of the gradient membrane.

Membranes	No. 1	No. 2	No. 3	No. 4	No. 5
Pore size, *d*	150 ± 4.8 μm	120 ± 3.9 μm	90 ± 3.2 μm	60 ± 2.6 μm	30 ± 2.2 μm
Wire diameter, 2*r*	48 ± 2.2 μm	48 ± 1.8 μm	50 ± 1.2 μm	50 ± 1.6 μm	56 ± 2.6 μm
d*/2*r	~3.13	~2.50	~1.80	~1.20	~0.54

* These single-pore-size membranes have similar 2*r* values. For the 150, 120 and 90 μm membranes, $d/2r > \sqrt{2}$; for the 60 μm membrane, $0.57 < d/2r < \sqrt{2}$; for the 30 μm membrane, $d/2r < 0.57$.

Table S2. Effects of H_2O addition to the precursor solution on the cell size and resultant sliding speed of the 90 μm membranes with different nanostructured coatings.

H_2O addition	0 g	0.5 g	1.0 g	2.0 g	4.0 g
Cell size	~0 μm	~0.14 μm	~0.85 μm	~0.63 μm	~0.45 μm
Sliding speed	0.19 ± 0.03 mm s^{-1}	0.20 ± 0.04 mm s^{-1}	0.28 ± 0.05 mm s^{-1}	0.26 ± 0.05 mm s^{-1}	0.24 ± 0.04 mm s^{-1}

* The cell size was statistically measured horizontally, vertically and diagonally across the SEM micrographs.

Table S3. Oil container heights above the oil/water interface for the gradient membrane and single-pore-size membrane at different device speeds.

Device speed		0.3 m s^{-1}	0.4 m s^{-1}	0.5 m s^{-1}	0.6 m s^{-1}
Gradient membrane (average pore size, 90 μm)	***h***	~1.0 cm	~1.3 cm	~1.7 cm	~2.2 cm
	H	1.1 cm	1.43 cm	1.87 cm	2.42 cm
Single-pore-size membrane (90 μm)	***h***	~1.2 cm	~1.6 cm	~2.1 cm	~2.7 cm
	H	1.32 cm	1.76 cm	2.31 cm	2.97 cm

* The height of the oil container (H) was set as $H = 1.1h$ (where h is the climbing height of the water current), such that water will not flow into the container during the collection process.

References

1. Brainerd, E. L. Caught in the Crossflow. *Nature* **2001**, *412*, 387-388.

2. Tuteja, A.; Choi, W.; Ma, M.; Mabry, J. M.; Mazzella, S. A.; Rutledge, G. C.; Mckinley, G. H.; Cohen, R. E. Designing Superoleophobic Surfacees. *Science* **2007**, *318*, 1618-1622.

3. Tian, D.; Chen, Q.; Nie, F.-Q.; Xu, J.; Song, Y.; Jiang, L. Patterned Wettability Transition by Photoelectric Cooperative and Aniscotropic Wetting for Liquid Reprography. *Adv. Mater.* **2009**, *21*, 3744-3749.